

Proton-rich two-dimensional defective Bi_2S_3 -derived nanosheets for boosting CO_2 electroreduction

Youzeng Li, Jialei Chen, Shan Chen, Tiantian Lu, Xuelong Liao, Tete Zhao, Fangyi Cheng, Huan Wang*

Key Laboratory of Advanced Energy Materials Chemistry (Ministry of Education), Renewable Energy Conversion and Storage Center (RECAST), Collaborative Innovation Center of Chemical Science and Engineering (Tianjin), College of Chemistry, Nankai University, Tianjin 300071, China



ARTICLE INFO

Keywords:
 2D Bi_2S_3 nanosheets
 Defects
 Sulfur dopants
 Protonation process
 CO_2 electroreduction

ABSTRACT

Bismuth (Bi)-based catalysts have attracted great attention in electrocatalytic CO_2 reduction into formate, but suffer from modest activity due to insufficient active sites and slow protonation process. Here, two-dimensional (2D) defect-rich Bi_2S_3 nanosheets are first achieved through chemical vapor sulfidization of Bi_2O_3 solids. It is found that the defects enable the stable immobilization of S heteroatoms into 2D Bi lattice. A combination of computational and experimental analyses reveal that S dopants can not only facilitate water dissociation to construct proton-rich surface, but also concentrate potassium cations to stabilize $^*\text{OCHO}$ intermediates. Further cooperating with defects, the $^*\text{OCHO}$ formation can be both kinetically and thermodynamically boosted. Remarkably, the constructed Bi_2S_3 nanosheets exhibit a high formate Faradaic efficiency (>90%) over a wide potential window and a high intrinsic stability over 200 h. The excellent performance in flow cell as well as promising solar-driven CO_2 electrocatalysis further demonstrate the great potential for practical implementation.

1. Introduction

Electrocatalytic carbon dioxide reduction reaction (ECO_2RR) into formate driven by renewable electricity provides a promising pathway to mitigate carbon emission issues while producing valuable chemicals [1–10]. Of particular, formate plays an important role in the chemical industry, hydrogen storage carrier and fuel cells. With the merits of low cost, nontoxicity and suppressed hydrogen evolution reaction (HER) activity, bismuth (Bi)-based catalysts have been extensively studied to electro-catalyze CO_2 into formate [11–13]. In this context, a wide variety of Bi-based precursors with designed morphologies have been developed to optimize the CO_2RR performance, including Bi nanoribbons [14,15], Bi nanotubes [16], Bi nanosheets [17], and Bi micro-particles [18].

Among them, 2D Bi-based electrocatalysts show unique merits owing to their ultrathin thickness and large surface area that facilitate accessible active sites and fast electron transfer. To further boost the CO_2RR activity, structural defects have been introduced into 2D Bi systems to activate CO_2 molecular and break the linear scaling relation of formation energy of intermediates [19]. For example, Mai et al. obtained Bi nanosheets with the edge defect sites coordinated with S heteroatoms

via electrochemical reconstruction of $\text{Bi}_{19}\text{Br}_3\text{S}_{27}$ nanowires [20], which can adjust the electronic structure of Bi to reduce $^*\text{H}$ adsorption sites and promote ECO_2RR selectivity. Despite the great progress, there is a big gap between the state-of-the-art CO_2RR performance and practical application levels, which needs further modification of catalysts.

Since the formation of formate intermediate ($^*\text{OCHO}$) requires the $^*\text{H}$ participation from H_2O dissociation, the insufficient proton feeding of pure Bi catalysts causes slow protonation process, limiting CO_2 conversion to formate. Most recent studies have revealed the introduction of S element can promote the H_2O dissociation and adsorb the generated $^*\text{H}$ under cathode potential [21,22], providing sufficient protons for promoting formation of $^*\text{COOH}$ intermediate, which is a critical step for determining CO_2 -to-CO activity and selectivity. However, the effect of proton feeding on formate formation still remains elusive. Thus, it is highly desirable to achieve appropriate Bi-containing precursors that can *in situ* immobilize S heteroatoms into the 2D Bi lattice. In comparison with the ternary layered compounds, the binary layered ones such as Bi_2S_3 attracts less attention. This is largely due to the special atomic structure of Bi_2S_3 that consists of ribbon-like Bi_4S_6 polymers linked together by intermolecular attraction (Fig. S1). The atomic scale ribbons building blocks are parallel to the c axis along [001] direction, usually

* Corresponding author.

E-mail address: huan.wang0520@nankai.edu.cn (H. Wang).

leading to one-dimensional structure with high aspect ratio [23], which makes it rather challenging to achieve 2D Bi₂S₃. To the best of our knowledge, there is rare report on the synthesis of 2D Bi₂S₃ as well as on 2D Bi₂S₃ for CO₂RR. While the covalent linkage between Bi and S is likely to be capable of anchoring S dopants into the 2D Bi lattice through defect/vacancy engineering without morphology reconstruction, which provides a new prototype to explore proton feeding effect via heteroatom doping.

Following the above lines, we present a novel and scalable approach for the synthesis of 2D defective Bi₂S₃ NSs through chemical vapor sulfurization of bulk Bi₂O₃ for efficient CO₂ electroreduction. It is found that the high-temperature sulfurization reaction can provide sufficient low-molecular sulfur to break the anisotropic growth of Bi₂S₃, thus enabling the growth of sheet-like Bi₂S₃. Comparative studies show that the multiple defects in Bi₂S₃ NSs can assist the stable immobilization of S heteroatoms into 2D Bi NSs during in situ transformation under cathode potential. Based on the catalyst model, we find that the S dopants enable construction of a proton-rich surface by facilitating H₂O dissociation, which is favourable for CO₂ activation and protonation for *OCHO intermediate generation. Moreover, potassium cations (K⁺) can be concentrated around S heteroatoms, which can further stabilize *OCHO intermediates. In combination with the surrounding defects, the intermediates (*OCHO) formation can be both kinetically and thermodynamically boosted. Consequently, the in situ constructed Bi₂S₃ NSs deliver a high Faradaic efficiency (>90%) for formate production over a wind potential window (-0.52 V~−1.16 V), as well as a high stability over 200 h of continuous operation. Meanwhile, it achieves a superior CO₂RR performance in the flow cell with large current density, high formate production rate and long-term durability. More impressively, a high solar-to-formate conversion efficiency of 13.9% is obtained in the full cell electrocatalysis powered by GaInP/GaInAs/Ge photovoltaic cell. This work provides a novel 2D Bi-based precursor for efficient CO₂RR and unravel the heteroatom doping effect on formate production.

2. Experimental section

2.1. Chemical reagents

Bismuth nitrate (Bi(NO₃)₃•5 H₂O, 99%), sulfur powder (99.9%), ethylene glycol, potassium bicarbonate (KHCO₃, 99.99%), potassium hydrogen phosphate (K₂HPO₄), potassium sulphate (K₂SO₄), potassium hydroxide (KOH, 95%) and sodium chloride (NaCl, 99.99%) were purchased from Shanghai Macklin Biochemical Co., Ltd. Argon (Ar, 99.999%), and carbon dioxide (CO₂, 99.999%) gas were purchased from Dongrun Co., Ltd.

2.2. Synthesis of bulk Bi₂O₃ dispersed in NaCl

10.0 g of commercial sodium chloride (NaCl) crystal was mixed with 1.0 g of commercial Bi (NO₃)₃•5 H₂O and then dissolved into 5.0 mL of ethylene glycol, followed by drying in a vacuum oven at 80 °C for 3 h. Finally, the as-obtained mixture was further annealed in air at 500 °C for 30 min to produce the light-yellow powder, thus achieving bulk Bi₂O₃ dispersed in NaCl (Bi₂O₃/NaCl powder).

2.3. Preparation of Bi₂S₃ Nanosheets (NSs)

The synthesis of Bi₂S₃ nanosheets was carried out in a home-built chemical vapor deposition (CVD) system equipped with two-zone furnace (LW-1100-30-2std) through sulfurization of the as-synthesized Bi₂O₃/NaCl powder at elevated temperatures, as schematically shown Fig. S2. Specifically, the sulfur powder and Bi₂O₃/NaCl were load into the hot center of the first zone and second zone. The system was pumped to a base pressure of 1 Pa to remove air. The temperature of the first zone was set as 120 °C, and the temperature of

second one was changing from 400 to 700 °C. Argon (Ar) was used as the carrier gas with the flow rate of 500 sccm. After 40 min of growth, the furnace was naturally cooled down to room temperature with the protection of Ar gas, black powder was obtained. Then NaCl was removed by water. After a sonication treatment in the mixed-solvent of water and isopropyl alcohol, uniform Bi₂S₃ NSs were achieved through a drying treatment.

2.4. Material characterizations

Scanning electron microscopy (SEM) images were collected using JSM-7500 F. Transmission electron microscopy (TEM) images were collected with Talos F200X G2. The aberration-corrected high-angle annular dark-field scanning TEM (HAADF-STEM) characterizations and electron energy loss spectroscopy (EELS) were carried out with JEM-ARM200F. Atomic force microscopy was performed with bruker icon. X-ray diffraction (XRD) patterns were recorded using a Smart Lab 9KW. X-ray photoelectron spectroscopy (XPS) analysis was conducted on Thermo Scientific with Al K Alpha ($\text{hv} = 1486.6 \text{ eV}$). X-ray absorption fine spectroscopy (XAFS) measurements were carried out using Beamline of TPS44A1 in National Synchrotron Radiation Research Center (NSRRC), Taiwan.

2.5. Electrocatalytic measurements

The CO₂ electroreduction experiments were carried out in a two-compartment electrochemical cell separated by anion exchange membrane (SELEMION, AGC Engineering Co., LTD) at ambient condition on an electrochemical workstation (CHI 660E) using a three-electrode configuration. To prepare working electrode, 10.0 mg of Bi₂S₃ NSs as pre-catalysts was dispersed in 2.0 mL of absolute ethanol containing 20 μL of 5 wt% Nafion under stirring to form a homogenous slurry. For H-type cell, the mixed slurry was casted onto carbon paper ($1 \times 1 \text{ cm}^2$). While for the flow cell, an air brush was employed to coat the slurry on the gas-diffusion electrode (GDE) with a mass loading of $\sim 1.0 \text{ mg cm}^{-2}$.

The CO₂ electrochemical reduction in H-type cell was conducted in CO₂-saturated 0.5 M KHCO₃ solution. A flow of 30 sccm CO₂ was continuously fed to the cathodic compartment during the experiment to obtain CO₂-saturated KHCO₃ electrolyte ($\text{pH} \approx 7.4$). All the potential readings were iR-corrected excepted noted. Platinum (Pt) mesh and saturated calomel electrode (SCE) were used as counter electrode and reference electrode, respectively. All potentials were converted to reversible hydrogen electrode (RHE) according to the following equation:

$$E (\text{vs. RHE}) = E (\text{vs. SCE}) + 0.244 \text{ V} + 0.0591 \times \text{pH}$$

Flow cell measurements were performed in a custom designed flow cell reactor. We used Bi₂S₃ NSs-loaded GDE ($1 \times 1 \text{ cm}^2$) as the working electrode, a piece of Pt mesh and Ag/AgCl as counter electrode and reference electrode, respectively. The catholyte was 1 M KOH. All potentials were converted to reversible hydrogen electrode (RHE) according to the following equation:

$$E (\text{vs. RHE}) = E (\text{vs. Ag/AgCl}) + 0.197 \text{ V} + 0.0591 \text{ V} \times \text{pH}$$

For the solar-driven full-cell measurements, a commercial three-junction GaInP/GaInAs/Ge solar cell ($1 \times 1 \text{ cm}^2$) with an open-circuit voltage (V_{oc}) of 2.5 V and a short-circuit current (I_{sc}) of 11.5 mA cm^{-2} was driven by a 300 W Xe lamp equipped with an AM 1.5 solar simulator (1 Sun), and the current-voltage curve was tested by Keithley 2400. RuO₂ loaded on carbon paper was used as the electrocatalyst for oxygen evolution reaction (OER). CO₂RR-OER electrolysis was performed in two-compartment cell powered by solar cell. The solar-to-formate (STF) conversion efficiency was calculated below:

$$\text{STF} = \frac{E_0 \times J \times \text{FE}_{\text{Formate}} \times S_{\text{electrode}}}{P_{\text{solar}} \times S_{\text{illuminated area}}}$$

Where E_0 is the equilibrium potential for CO_2 reduction to HCOOH and water oxidation and here is 1.43 V. J is the working current density. $S_{\text{electrode}}$ is the geometric area of working electrode and $S_{\text{illuminated area}}$ is the illuminated area of solar cell. P_{solar} represents the energy intensity and here is 100 mW cm^{-2} .

The gas-phase products were detected by a gas chromatograph (GC) equipped with a flame ionization detector (FID) and a thermal conductivity detector (TCD). Liquid products were analyzed by proton nuclear magnetic resonance ($^1\text{H NMR}$) with dimethyl sulfoxide (DMSO) as an internal standard, which was calculated based on the following equation:

$$\text{FE}_{\text{HCOO}^-} (\%) = \frac{Q_{\text{HCOO}^-}}{Q_{\text{total}}} \times 100\% = \frac{n_{\text{HCOO}^-} \times N \times F}{j \times t} \times 100\%$$

where n_{HCOO^-} is the amount of formate determined by $^1\text{H NMR}$, $N=2$ is the electron transfer number to form a molecule of formate, F is the Faraday constant ($96,500 \text{ C mol}^{-1}$), j is the total current, and t is the electrolysis time.

2.6. Electrochemical *in situ* ATR-FTIR

Electrochemical *in situ* attenuated total reflection Fourier-transform infrared (ATR-FTIR) spectra were performed on a Fourier transform infrared spectrometer (FTIR, Nicolet iS50) equipped with a liquid-nitrogen-cooled MCT detector. Bi_2S_3 NSs, commercial Bi_2S_3 and pure Bi on Si prisms covered with Au film were employed as working electrode. Saturated calomel electrode (SCE) and Pt wires were served as reference electrode and counter electrode, respectively. All experiments were performed at ambient conditions and the IR spectra were recorded at applied potentials in CO_2 -saturated 0.5 M KHCO_3 solution.

2.7. Electrochemical *in situ* Raman

In situ Raman test was carried out in a homemade cell with a three-electrode configuration at applied potentials in CO_2 -saturated 0.5 M KHCO_3 solution under ambient conditions. Saturated Ag/AgCl and a Pt wire were used as the reference and counter electrode, respectively. *In situ* Raman spectra were recorded on a confocal Raman spectroscopy (LabRAM HR Evolution) using a 633 nm laser source.

2.8. Computational details

We have employed the Vienna Ab initio Simulation Package (VASP) to perform all density functional theory (DFT) calculations within the generalized gradient approximation (GGA) using the Revised Perdew-Burke-Ernzerhof (PBE) functional. We have chosen the projected augmented wave (PAW) potentials to describe the ionic cores and take valence electrons into account using a plane wave basis set with a kinetic energy cutoff of 450 eV. We used the implicit solvation model implemented in VASP sol to explicitly calculate Esol. The DFT-D3 empirical correction method was employed to describe van der Waals interactions. Geometry optimizations were performed with the force convergency smaller than $0.05 \text{ eV}/\text{\AA}$. Monkhorst-Pack k-points of $2 \times 2 \times 1$ was applied for all the calculations. Half atoms at bottom are fixed in all the calculations. The free energy changes (ΔG) of each elementary reaction step were calculated using the computational hydrogen electrode (CHE) model. In this model, the chemical potential is equal to the energy of half of the gas-phase H_2 at 0 V vs reversible hydrogen electrode (RHE). The electrode potential, U verse RHE, is taken into consideration by adding $-eU$ when an electron transforming step occurs. That is $G(U) = G(0 \text{ V}) - neU$, where e is the elementary charge of an electron, n is the number of proton-electron pairs transferred, and U is the applied potential. The

Gibbs free energy was calculated by the following equation:

$$\Delta G = \Delta E + \Delta E_{\text{ZPE}} - T\Delta S + \Delta \int CpdT$$

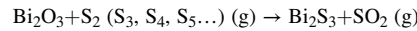
Where the value of ΔE , ΔE_{ZPE} and ΔS denotes the changes of DFT energy, the zero-point energy and the entropy at 300 K, respectively.

The S-doped defective Bi, defective Bi and pure Bi model were structured for DFT calculations. The supercell of Bi (012) was $19.19 \text{ \AA} \times 18.44 \text{ \AA}$, and a vacuum space of 15 \AA to avoid interactions between slabs. The defective Bi (012) is a vacancy surface, which is one Bi vacancy on the surface. The S-doped defective Bi is one S atom doped d-Bi (012). It's worth noting that this does not transform the structures of both the defective Bi (012) and the S-doped defective Bi (012), still maintains the Bi (012) lattice.

3. Results and discussion

3.1. Catalysts preparation and characterization

The synthesis of 2D Bi_2S_3 NSs was conducted in a home-built low-pressure chemical vapor deposition system and the conversion process from bulk Bi_2O_3 solids to layered Bi_2S_3 nanosheets is schematically illustrated in Fig. 1. Briefly, the as-prepared $\text{Bi}_2\text{O}_3/\text{NaCl}$ powder was placed in the hot center of the tube furnace (Fig. S2, see details in the Supporting Information), and sulfur powder was placed upstream low-temperature region. The bulk Bi_2O_3 was then annealed in the atmosphere of sulfur vapor carried by Ar gas at 650°C for 40 min. During the high-temperature annealing, the sulfurization of Bi_2O_3 follows the chemical reaction below:



At high temperature, the concentration of low-molecular sulfur (S_2) sharply increases and instantly inserts into the bulk Bi_2O_3 . The Bi-O bonds thus can easily react with S vapor, resulting in Bi-O bond cleavage and Bi-S bond formation. In this scenario, continuous reaction occurs within the Bi_2O_3 block due to the rapid diffusion of low-molecular sulfur. Also, the insertion of sulfur vapor and ejection of gashouse SO_2 can break van der Waals forces to prevent the stacking of thin layers. When Bi-S bonds are formed, rapid diffusion rate of sulfur molecules breaks the anisotropy nature of Bi_2S_3 growth, which can avoid the formation of ribbon-like Bi_4S_6 polymers linked along [001] direction for one-dimensional structure. Thus, the bulk Bi_2O_3 can successfully convert into sheet-like structure of Bi_2S_3 through a facile chemical vapor sulfurization process (Fig. 1b, c). X-ray diffraction (XRD) measurements show the nearly complete transformation of Bi_2O_3 to Bi_2S_3 (Fig. S3). It is found that the evolution of Bi_2S_3 NSs strongly depends on the sulfurization temperature (Fig. S4), which can be explained by the insufficient SO_2 release at low temperatures that cannot effectively insert the solid.

The morphology of the as-prepared Bi_2S_3 NSs was examined by transmission electron microscopy (TEM). Fig. 1d shows a low-resolution TEM image of Bi_2S_3 NS, where the transparency confirms the ultrathin 2D nature of Bi_2S_3 NSs. The lattice spacing of 0.254 nm in aberration-corrected high-angle annular dark-field scanning TEM (HAADF-STEM) image corresponds to the (240) plane of Bi_2S_3 (Fig. 1e). Moreover, many dislocations and distortions marked by dashed circles are observed in both HAADF-STEM and high-resolution TEM (HRTEM) images (Fig. S5), which suggest the existence of rich defects in Bi_2S_3 NSs, possibly due to destruction of lattice caused by SO_2 ejection at high temperature. Along the arrows in Fig. 1e, the peak intensity profile of nine atoms was obtained, as shown in Fig. S6. The sudden decrease in the atomic column intensity corresponds to the presence of Bi defect. Moreover, the clear diffraction spots in the fast Fourier transform pattern in Fig. S7 manifest the monocrystalline nature of Bi_2S_3 NSs, indicating the defects are from disordered atomic arrangement on the basal plane, rather than from the grain boundaries or stacking fault of interlayer. The cross-sectional

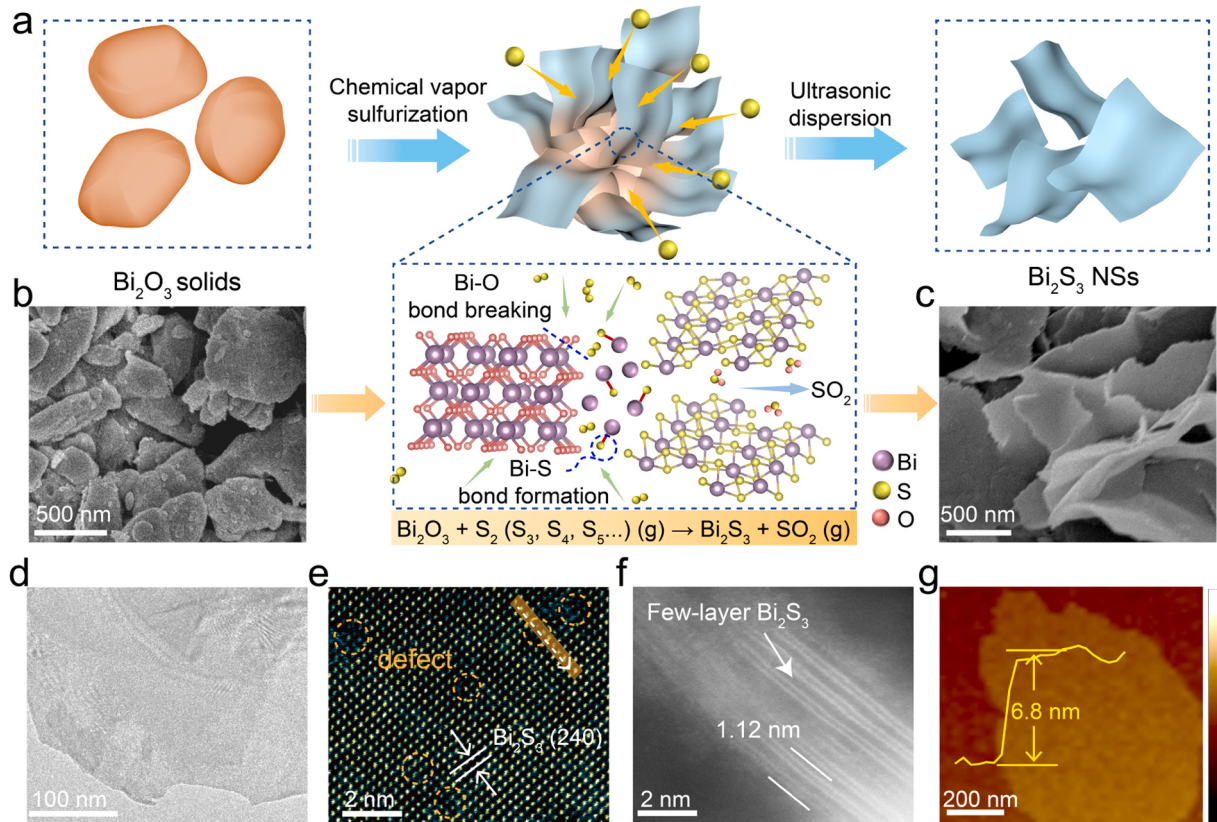


Fig. 1. (a) Schematic of the chemical vapor sulfurization process for the conversion of bulk Bi_2O_3 to 2D Bi_2S_3 NSs. SEM images of bulk Bi_2O_3 (b) and Bi_2S_3 NSs (c). (d) TEM and (e) aberration-corrected HAADF-STEM images of Bi_2S_3 NSs. The orange dashed circles indicate the defects in Bi_2S_3 . (f) Cross-sectional TEM image of few-layer Bi_2S_3 NSs. (g) AFM image and corresponding thickness profile of Bi_2S_3 NSs.

image in Fig. 1f reveals the few-layer structure with a unit cell thickness of 1.12 nm. The thickness of the Bi_2S_3 NSs was further determined by atomic force microscopy (AFM). As depicted in Fig. 1g, the AFM image and height profile of Bi_2S_3 NSs exhibit a flat surface with a uniform thickness of ~6.8 nm, corresponding to sixfold unit cell thickness [24]. Thus, by optimizing the growth temperature, we realize the synthesis of 2D ultrathin Bi_2S_3 NSs with rich defects. It is worth mentioning that this strategy enables the gram-scale production of Bi_2S_3 NSs in one batch (Fig. S8).

3.2. Electrochemical CO_2 reduction measurement

The CO_2 electroreduction performance was first evaluated in 0.5 M CO_2 -saturated KHCO_3 solution using H-type cell. All potentials are referred to the reversible hydrogen electrode (RHE) excepted noted. Commercial Bi_2S_3 (c- Bi_2S_3) and pure Bi (p-Bi) were used as control samples (Fig. S9). Note that Bi_2S_3 here serves as the pre-catalyst, and would transform to metallic Bi, as discussed later. As revealed by the polarization curves in Fig. S10, the higher current densities were obtained in the CO_2 -saturated electrolyte than in Ar atmosphere, confirming the occurrence of CO_2RR . Besides, the Bi_2S_3 NSs afford a smaller onset potential and larger current density than those of c- Bi_2S_3 and p-Bi, demonstrating its superior CO_2RR activity. Impressively, the formate Faradaic efficiency (FE) over Bi_2S_3 NSs exceeds 90% in a wide potential window and reaches the maximum value of 98.6% at -0.86 V (Fig. 2a), while the FE for both CO and H_2 is below 10% (Fig. S11). In stark contrast, c- Bi_2S_3 and p-Bi both display the maximum FE of 66.1% and 81.3%, respectively, obviously smaller than that of Bi_2S_3 NSs. Correspondingly, Bi_2S_3 NSs achieve a much higher partial current density for formate production (Fig. S12). Besides, the smaller resistance of charge transfer (R_{ct}) implies the rapid electron transfer (Fig. S12, Table S1),

consistent with the lower Tafel slope (Fig. S13), further demonstrating the boosted intrinsic activity of Bi_2S_3 NSs for CO_2RR . The Bi_2S_3 NSs present the largest surface roughness factor (Fig. S14), which is estimated by comparing the measured double-layer capacitance derived from cyclic voltammetry (CV) curves with the value for bare carbon paper, reflecting that there are more effective active sites in 2D Bi_2S_3 NSs. More importantly, the Bi_2S_3 NSs deliver an ultra-stable current density over 200 h of continuous catalysis at -0.93 V with an average formate FE above 90% (Fig. 2b). The CO_2RR durability related to structural stability is an important criterion. To this end, we compared the pristine activity and durability in H-type cell using KHCO_3 electrolyte. The superb durability far outperforms the most previously reported formate-selective catalysts in the neutral media (Fig. 2c, Table S2), a strong hint that the reconstructed Bi_2S_3 NSs can remain stable during the continuous electrocatalysis.

To assess the commercial viability of Bi_2S_3 NSs, the CO_2RR performance was further measured in a flow cell reactor with gas-diffusion electrode in 1 M KOH electrolyte. Without the limitation of CO_2 mass transport, the Bi_2S_3 NSs in flow cell show a much larger current density than that in H-type cell, where a current density up to $-721.3 \text{ mA cm}^{-2}$ is achieved at -1.54 V (Fig. 2d). Likewise, formate overwhelmingly dominates the CO_2RR products across the wide potential range from -0.73 V to -1.27 V (Fig. 2e). The highest FE of formate reaches 96.2% at -1.1 V with a profitable current density of $-360.0 \text{ mA cm}^{-2}$, corresponding to a formate partial current density of $-346.3 \text{ mA cm}^{-2}$ (Fig. 2f). At a higher potential of -1.27 V, the formate FE still remains 96.0% with a partial current density of $-451.0 \text{ mA cm}^{-2}$, corresponding to a formate production rate (PR) of $8.4 \text{ mmol h}^{-1} \text{ cm}^{-2}$. The formate PR and FE can be comparable to the most previously reported formate-selective electrocatalysts in flow cell using 1 M KOH (Fig. S16, Table S3). Notably, the Bi_2S_3 NSs maintain the high FE for formate

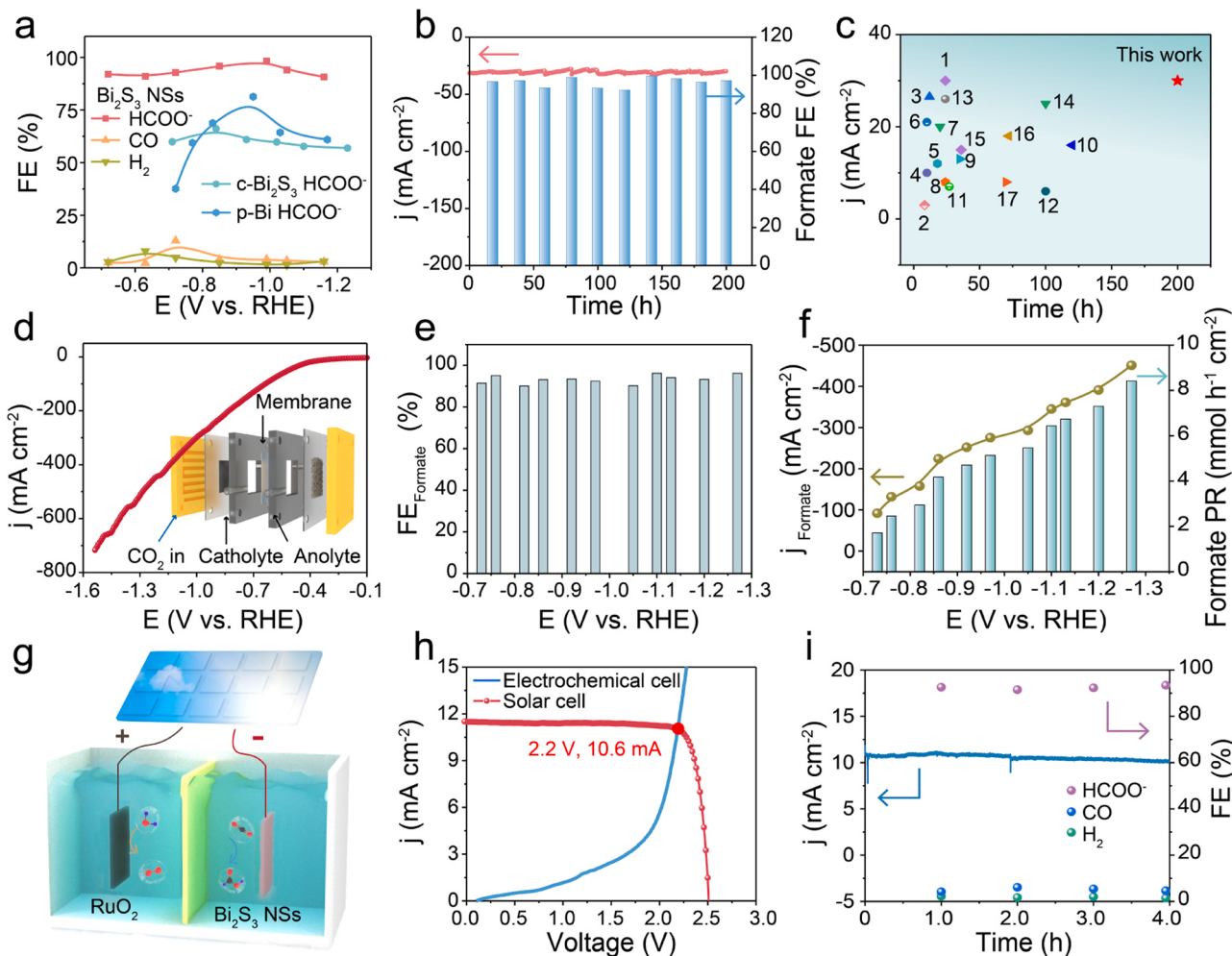


Fig. 2. (a) Potential-dependent Faradaic efficiencies of formate over Bi₂S₃ NSs, c-Bi₂S₃, and p-Bi. (b) Long-term electrocatalysis of Bi₂S₃ NSs for more than 200 h of continuous operation at -0.93 V. (c) Comparison of pristine activity and durability of Bi₂S₃ NSs with those of recently reported formate-selective electrocatalysts in CO₂-saturated KHCO₃ solution using H-type cell (pH≈7.0) [15,25–40]. Nos. 1–17 indicate values from refs 15, and 25–40, respectively. (d) LSV curve of Bi₂S₃ NSs in flow cell. Inset: the schematic illustration of flow cell for CO₂RR. (e) The Faradaic efficiency of formate at each applied potential in flow cell. (f) The corresponding formate current density and production rate. (g) Schematic illustration of the solar-driven CO₂RR/OER full cell. (h) Current density-voltage curve of the solar cell under AM 1.5 G illumination and the corresponding polarization curve of full cell. (i) Current density and Faradaic efficiency of formate at 2.2 V for the full cell over 4 h of continuous electrocatalysis.

(>96%) after 50 h of continuous electrocatalysis with a high current density of -210.0 mA cm⁻² (Fig. S17). The above results manifest the superior CO₂RR activity and stability of reconstructed Bi₂S₃ NSs.

Furthermore, we fabricated the solar-driven full cell by using Bi₂S₃ NSs as cathode catalyst for CO₂RR and RuO₂ as anode catalyst for oxygen evolution reaction (OER), respectively, as shown in Fig. 2g. A commercial three-junction GaInP/GaInAs/Ge solar cell was employed to harvest the light from a 100 mW cm⁻² (1 Sun) solar simulator that can produce an open-circuit voltage of 2.5 V and a short-circuit current of 11.5 mA. According to the intersection point in Fig. 2h, the working voltage and current can be determined to be ~2.2 V and ~10.6 mA cm⁻², respectively. Over 4 h of solar-driven electrocatalysis, a stable current density exceeding 10.0 mA cm⁻² was achieved with a formate FE above 90% (Fig. 2i). Accordingly, the solar-to-formate conversion efficiency was calculated to be 13.9% (see details in the Supporting Information). More inspiringly, CO₂RR-OER full cell electrocatalysis driven by Si solar cell under natural sunlight is realized (Fig. S18), holding great promise for converting CO₂ into valuable fuels with renewable energy.

3.3. The structure evolution of catalysts

To understand the actual active moieties, the structure evolution of Bi₂S₃ NSs was first monitored by XRD at -0.90 V (Fig. S19). After 1 min of electroreduction, the diffraction peaks indexed to rhombohedral phase Bi (PDF No. 44–1246) appears, indicating the fast transformation from Bi₂S₃ to Bi. After 60 min, the characteristic peaks belonging to Bi₂S₃ completely disappears and all patterns are assigned to metallic Bi, similar to the reported results [41]. To further probe the stable catalyst morphology and compositions in CO₂RR, a series of characterizations were conducted on 2D Bi₂S₃ NSs after 20 hours of reduction at -0.90 V, ensuring that 2D Bi₂S₃ have been completely evolved into Bi NSs. The HRTEM image of Bi₂S₃ NSs after CO₂RR display a lattice spacing of ~0.33 nm, corresponding to the (012) plane of metallic Bi (Fig. 3a, S20). The defective Bi₂S₃ NSs not only retain the defects, but also well maintain the 2D nanosheet-like morphology after electroreduction to metallic Bi, as shown in Figs. S21. The fast Fourier transform pattern in Fig. S22 exhibits a set of diffraction spots assigned to the (012) and (104) planes of metallic Bi.

Furthermore, energy-dispersive X-ray spectroscopy (EDS) mapping for the Bi₂S₃ NSs after CO₂RR was conducted to analyze the chemical compositions, which reveal the coexistence of Bi and S elements with a

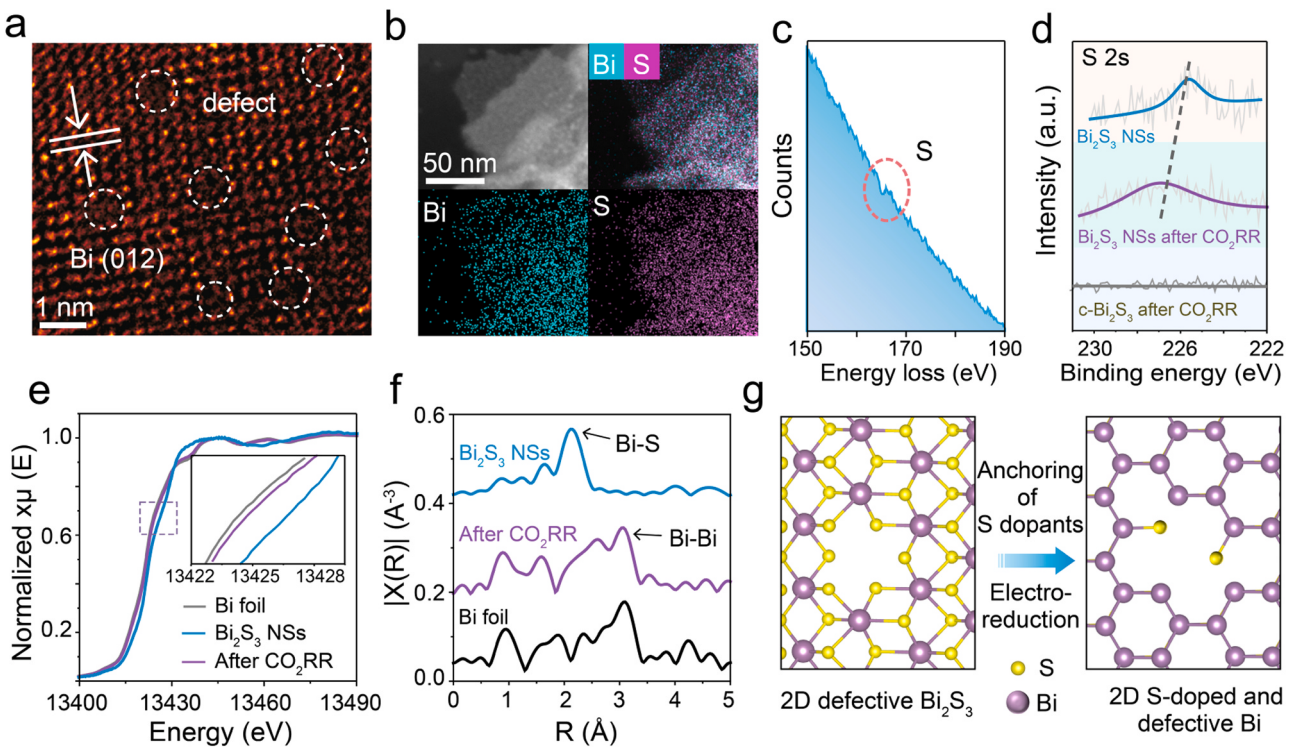


Fig. 3. (a) HRTEM image, (b) EDS mappings and (c) EELS spectrum of Bi_2S_3 NSs after CO_2RR . The defects are marked by white dashed circles in (a). (d) XPS spectra of S 2 s for Bi_2S_3 NSs, c- Bi_2S_3 and Bi_2S_3 NSs after CO_2RR . (e) Bi L₃-edge XANES spectra of Bi foil, Bi_2S_3 NSs and Bi_2S_3 NSs after CO_2RR . (f) The K₃-weighted Fourier transformation of the EXAFS spectra. (g) Schematic diagram of the structural evolution from defective Bi_2S_3 NSs to S-doped Bi NSs with defects.

uniform distribution across the nanosheets (Fig. 3b). Moreover, an inconspicuous peak at ~ 165.2 eV assigned to S elements appears in the electron energy loss spectroscopy (EELS), illustrating the survival of sulfur species in the Bi lattice after CO_2RR (Fig. 3c). This can be further supported by the obvious S 2 s XPS peak at ~ 226.8 eV in Fig. 3d, which shows a negative shift relative to the original Bi_2S_3 NSs due to the enhanced Bi-S bond strength. Conversely, no S 2 s XPS signal can be detected in the commercial Bi_2S_3 after CO_2RR due to the absence of defects as anchoring site in commercial Bi_2S_3 (Fig. S24). These results collectively illustrate that the 2D defective Bi_2S_3 NSs are in situ converted to 2D metallic Bi with the incorporation of both defects and S dopants, which then serve as the active species for the long-term CO_2 electrocatalysis.

X-ray absorption fine structure spectroscopy (XAFS) was further conducted at the Bi L-edge to probe chemical state and the local environment. The X-ray absorption near-edge structure (XANES) spectra show that the absorption-edge position of Bi_2S_3 NSs after CO_2RR is similar to Bi foil, indicating the complete reduction of Bi_2S_3 to metallic Bi (Fig. 3e). Besides, in the extended X-ray absorption fine structure (EXAFS) spectra of Bi_2S_3 -derived sample, the major peak located at ~ 2.1 Å and ~ 3.09 Å correspond to the Bi-S bond and Bi-Bi bond, respectively (Fig. 3f), suggesting the reservation of Bi-S bonds and formation of Bi-Bi bonds after transformation of Bi_2S_3 to metallic Bi. Moreover, we further conducted the in situ Raman characterization under varied reduction potential (Figs. S25, S26). There appear two Raman characteristic peaks at ~ 71.0 cm⁻¹ and 97.0 cm⁻¹, which can be attributed to the Bi-Bi stretching mode. Besides, the Bi-S peak at around ~ 182.0 cm⁻¹ remains stable upon cathode potential. Based on the above analysis, it can be concluded that the 2D defective Bi_2S_3 NSs undergo in situ dynamic reconstruction during the electrocatalytic CO_2RR , leaving defects and partial S heteroatoms into the 2D Bi lattice. Notably, previous studies have shown that S elements of metal sulphides are inclined to completely dissolve into the electrolyte during CO_2RR [41]. The possible reason for the S existence in 2D defective Bi_2S_3 NSs is

that the lattice defects provide space to anchor the surrounding sulfur atoms, as schematically illustrated in Fig. 3g.

3.4. CO_2RR mechanism over sd-Bi catalyst

To further gain an insight into the CO_2RR mechanism, in situ electrochemical attenuated total reflection Fourier-transform infrared (ATR-FTIR) spectra were conducted to monitor the intermediates (Fig. S27). For simplicity, the defective Bi_2S_3 NS after electroreduction with S-doping and defects is denoted as sd-Bi. Meanwhile, the commercial Bi_2S_3 after reduction is also studied and denoted as c-Bi. According to XRD results in Fig. S28, the following sd-Bi and c-Bi represent the samples with 2 h of activation. As shown in Fig. 4a, the vibration of O-C-O in two-oxygen bridged as-signed to formate intermediate ($^*\text{OCHO}$) is detected at ~ 1380 cm⁻¹ and gradually increases as the potential negatively shifts. In comparison, the weak characteristic peaks of $^*\text{OCHO}$ intermediates in the two other control samples demonstrate that introduction of S heteroatoms and defects in sd-Bi can promote the $^*\text{OCHO}$ intermediate production. Then the formation free energies of $^*\text{OCHO}$ intermediate on different samples are compared with DFT calculations and the corresponding models are displayed in Fig. S29. The formation free energy of $^*\text{OCHO}$ intermediate on sd-Bi is 0.23 eV, which is apparently smaller as compared to p-Bi surface (0.417 eV) and defective Bi (d-Bi) surface (0.328 eV), as shown in Fig. 4b. This further confirms that the presence of S heteroatoms and defects can greatly stabilize $^*\text{OCHO}$ intermediate. To clearly show the charge transfer between the $^*\text{OCHO}$ intermediate and Bi electrocatalyst, we also compared the differential charge density (Fig. 4c). Relative to the d-Bi and p-Bi, the sd-Bi can transfer more electrons for $^*\text{OCHO}$, well explaining the obvious decrease in the formation free energy for $^*\text{OCHO}$. To figure out the catalytic dynamics, the density of states (DOS) over sd-Bi, d-Bi, and p-Bi with adsorbed $^*\text{OCHO}$ intermediate were calculated (Fig. 4d). The increased DOS intensity of sd-Bi near the Fermi level is expected to provide more charge carriers, which will participate in the catalytic

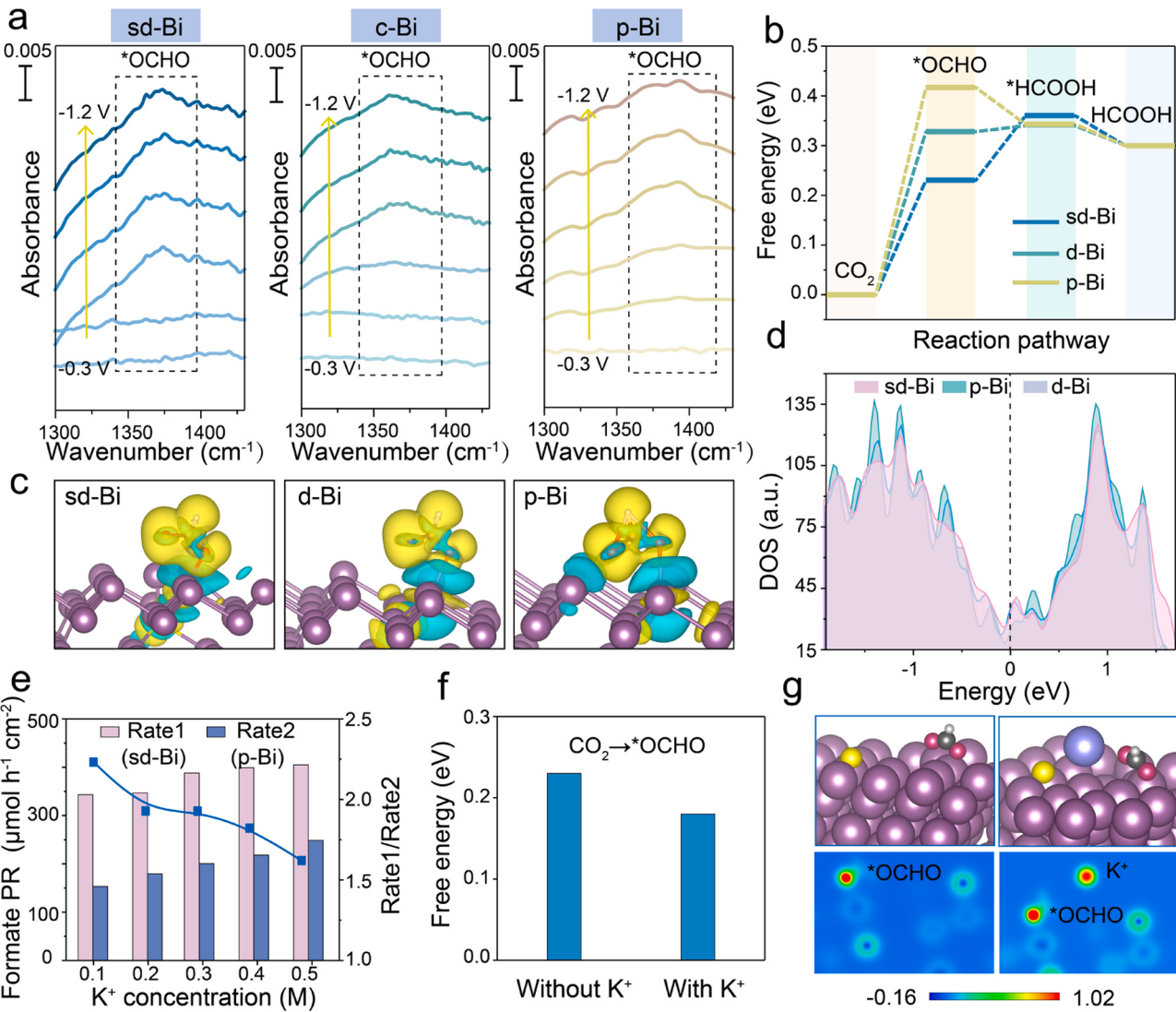


Fig. 4. (a) In situ ATR-FTIR spectra of sd-Bi c-Bi and p-Bi. (b) Calculated free-energy diagrams for CO_2 RR over sd-Bi, d-Bi, and p-Bi. Differential charge density (c) and DOS (d) of sd-Bi, d-Bi and p-Bi with adsorbed *OCHO. Yellow indicates electron accumulation, and cyan denotes electron deletion. (e) Formate PR and the ratio of rate over sd-Bi (R1) and p-Bi catalyst (R2) in electrolyte with different KHCO_3 concentrations at -0.9 V . (f) Gibbs free energy of CO_2 to *OCHO with or without of K^+ . (g) Optimized configurations of *OCHO intermediate and corresponding volume slice of calculated charge densities over sd-Bi catalyst with or without the presence of adsorbed K^+ .

reaction and facilitate rapid charge transfer kinetics for enhanced CO_2 RR performance. Therefore, binding S heteroatoms to the vicinity of defect sites can effectively accelerate *OCHO intermediate formation.

Besides, due to non-covalent Coulomb interactions, the S^{2-} is inclined to adsorb alkali metal cations in the electrolyte. On the basis, we furthered the study of K^+ adsorption effect on CO_2 RR performance by varying the KHCO_3 concentration from 0.5 M to 0.1 M. As shown in Fig. 4e, the formate PR of sd-Bi (denoted as Rate 1) is higher than that of p-Bi catalyst (denoted as Rate 2) regardless of the KHCO_3 concentration. Impressively, the value of Rate1/Rate2 increases to 2.2 as the K^+ concentration changes from 0.5 to 0.1 M, evidencing strong absorption ability of S species with K^+ . The concentration of surface-adsorbed K^+ was evaluated by ion chromatography, which shows that the absorption capability of sd-Bi with K^+ is around three-fold stronger than that of p-Bi (Fig. S30). Therefore, the sd-Bi surface can concentrate K^+ due to the strong absorption ability between sulfur species and K^+ , which further decreases the reaction free energy of CO_2 to *OCHO, as confirmed by DFT calculations in Fig. 4f. Volume slice of calculated charge densities in Fig. 4g displays more electron density on *OCHO in the presence of adsorbed K^+ , again confirming the better stabilization ability of *OCHO.

3.5. S doping effect on CO_2 RR

Since there are few studies on heteroatom-doped Bi electrocatalysts, we meticulously explored the S-doping effect on CO_2 RR behavior. Firstly, we employed H_2O and D_2O as the solvent to explore the H-D kinetic isotope effect (KIE). As illustrated in Fig. 5a, when D_2O was used to replace H_2O in 0.5 M KHCO_3 electrolyte, the formate PR decreases from 843.0 to 494.0 $\mu\text{mol h}^{-1} \text{cm}^{-2}$ on sd-Bi. The KIE was calculated to be 1.7. The same result was obtained on p-Bi with a value from 554.0 to 310.0 $\mu\text{mol h}^{-1} \text{cm}^{-2}$ (KIE=1.8). Thus, the H_2O dissociation affects the rate determining step for formate formation. This can be further supported by the highest formate PR in the electrolyte containing Cs^+ as compared to those in K^+ and Na^+ (Fig. S31), where the strongest Coulomb force between electronegative S heteroatoms (S^{2-}) and $\text{Cs}^+(\text{H}_2\text{O})_n$ complexes is the best for H_2O dissociation to form adsorbed hydrogen intermediate (H^*) towards *OCHO formation [22].

Considering that the energy barrier of water dissociation positively increases with electrolyte pH, we further studied CO_2 RR behavior in different kinds of electrolytes, i.e., K_2HPO_4 , KHCO_3 , and K_2SO_4 , with different local pH at cathode/electrolyte interface ($\text{K}_2\text{HPO}_4 < \text{KHCO}_3 <$

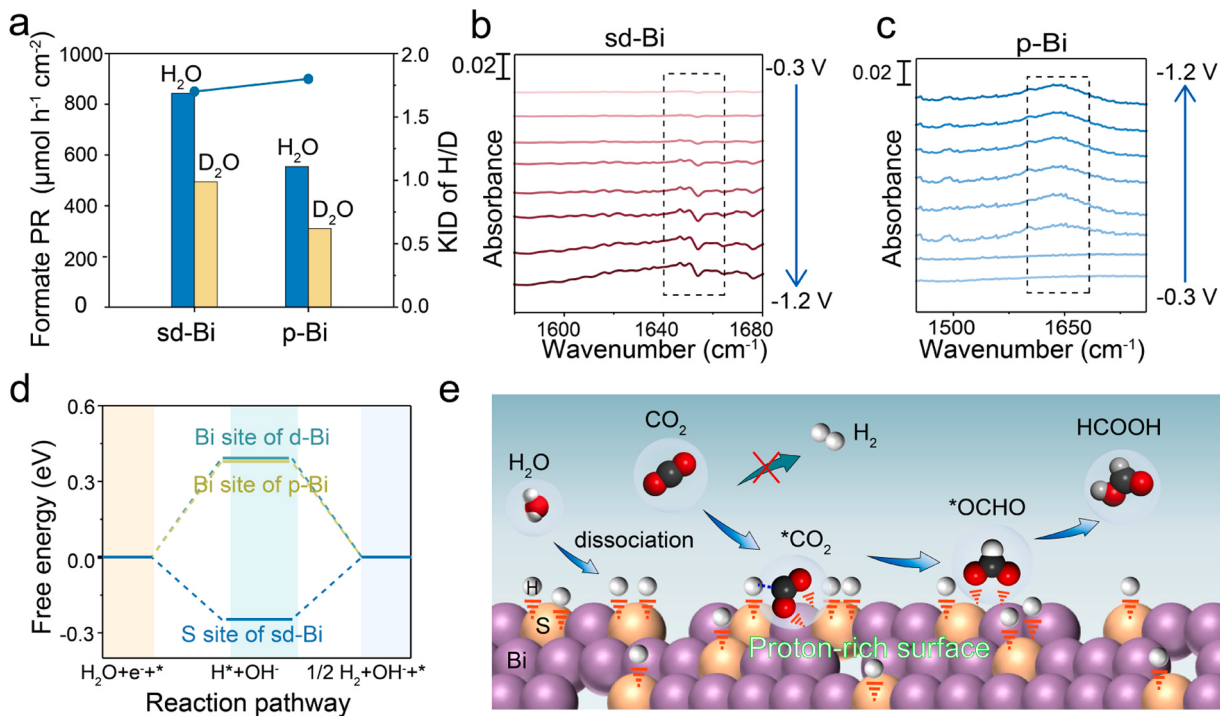


Fig. 5. (a) KIE of H–D over sd-Bi and p-Bi catalyst at -0.9 V. (b–c) In situ ATR-FTIR spectra at different applied potentials over sd-Bi and p-Bi catalyst. (d) Gibbs free energy for the formation of $^{*}\text{H}$ on S site of sd-Bi, Bi site of d-Bi and p-Bi. (e) The proposed reaction mechanism for CO₂RR over sd-Bi with proton-rich surface to stabilize $^{*}\text{OCHO}$ for CO₂ reduction to formate.

K₂SO₄) [42]. In comparison with sd-Bi, the p-Bi catalyst shows an obvious decrease in formate PR upon changing electrolyte from K₂HPO₄ to KHCO₃ and K₂SO₄ (Fig. S32), indicating that the S heteroatoms can accelerate the H₂O dissociation. On the basis, in situ ATR-FTIR was conducted to elucidate the S-doping effect on H₂O activation. As shown in Fig. 5b–c and S33, for sd-Bi sample, the peak at $\sim 1650 \text{ cm}^{-1}$ assigned to adsorbed H₂O is negative and shows a continuous decrease as potential negatively shifts, implying continuous H₂O consumption during CO₂RR. Conversely, the p-Bi and c-Bi both present positive and stable peaks as potential changes, suggestive of H₂O accumulation to release proton on the catalyst surface.

To further identify the S dopants are the active sites for H₂O decomposition, we compared the formation free energy for $^{*}\text{H}$ species on different electrocatalysts with density functional theory (DFT) calculations. As shown in Fig. 5d and the adsorption structures in Fig. S34, the formation free energy of $^{*}\text{H}$ on S site of sd-Bi is -0.25 eV, apparently smaller than that on Bi site of defective Bi (d-Bi) and p-Bi (0.39 eV and 0.38 eV), confirming that S dopants are responsible for the H₂O dissociation and promote CO₂ electroreduction by feeding protons for $^{*}\text{OCHO}$ intermediate formation. Combined with the above experimental and calculation results, S dopants in Bi lattice are beneficial for H₂O dissociation, thereby leading to a proton-rich Bi catalysts during CO₂RR, facilitating CO₂ activation and protonation, as shown in Fig. 5e.

4. Conclusions

In conclusion, we have developed a novel and scalable approach for converting Bi₂O₃ solids into 2D defective Bi₂S₃ NSs via a simple chemical vapor sulfurization method towards enhanced CO₂ electro-reduction. Our studies reveal that the defects in the as-received 2D Bi₂S₃ NSs can well prevere during the dynamic reconstruction, which enable the immobilization of sulfur species into the Bi lattice, thus achieving 2D defect-rich S-doped Bi nanosheets. It is found that the S dopants enhance water dissociation to release sufficient protons for a proton-rich surface, which favors $^{*}\text{OCHO}$ formation. Further collaborating with surrounding

defects, the formation of $^{*}\text{OCHO}$ is both kinetically and thermodynamically boosted. As a result, the reconstructed Bi₂S₃ NSs achieve an excellent CO₂RR performance with a formate Faradaic efficiency above 90% over a wide potential window ($-0.52 \text{ V} \sim -1.16 \text{ V}$) and a high stability over 200 h of continuous electrocatalysis without decay. More encouragingly, the 2D defect-rich S-doped Bi nanosheets exhibits near-unity formate selectivity, remarkable production rate and superior stability under ultrahigh current densities in flow cell. The CO₂RR/OER full cell powered by solar energy also demonstrates the practical viability. Our work provides a new type of Bi-based catalysts to realize efficient CO₂ electroreduction and offers an ideal platform to reveal the heteroatom effects on CO₂RR behavior.

CRediT authorship contribution statement

Youzeng Li: Conceptualization, Methodology, Experiments, Formal analysis, Investigation, Writing-original draft. **Jialei Chen, Shan Chen, Tiantian Lu, Xuelong Liao and Tete Zhao:** Investigation and Formal analysis. **Fangyi Cheng:** Writing-review & editing. **Huan Wang:** Conceptualization, Writing-review & editing, Investigation, Supervision, Funding acquisition.

Authorship statement

Y.L. and **H.W.** conceived the original idea and designed all the experiments. **Y.L.** carried out the experiments and analyzed the experimental data with the help of **J.C., S.C., T.L., X.L. and T.Z.** **Y.L.** and **H.W.** co-wrote the paper. **H.W.** supervised the project. All authors were involved in discussion of the experimental results and preparing of the manuscript.

Declaration of Competing Interest

The authors declare that they have no known competing financial interests or personal relationships that could have appeared to influence

the work reported in this paper.

Data availability

No data was used for the research described in the article.

Acknowledgements

We acknowledge the support from the National Natural Science Foundation of China (No. 22375103, 22105107), Ministry of Science and Technology of China (No. 2021YFA1201900) and the Fundamental Research Funds for the Central Universities. We are also grateful to Dr. Yan Zhang for the help in the measurement of FTIR (Nicolet iS50).

Appendix A. Supporting information

Supplementary data associated with this article can be found in the online version at [doi:10.1016/j.apcatb.2024.123874](https://doi.org/10.1016/j.apcatb.2024.123874).

References

- [1] P. De Luna, C. Hahn, D. Higgins, S.A. Jaffer, T.F. Jaramillo, E.H. Sargent, What would it take for renewably powered electro-synthesis to displace petrochemical processes? *Science* 364 (2019) 350.
- [2] L. Ge, H. Rabiee, M. Li, S. Subramanian, Y. Zheng, J.H. Lee, T. Burdyny, H. Wang, Electrochemical CO₂ reduction in membrane-electrode assemblies, *Chem* 8 (2022) 663–692.
- [3] M.B. Ross, P. De Luna, Y. Li, C.-T. Dinh, D. Kim, P. Yang, E.H. Sargent, Designing materials for electrochemical carbon dioxide recycling, *Nat. Catal.* 2 (2019) 648–658.
- [4] P. Yang, M. Gao, Enrichment of reactants and intermediates for electrocatalytic CO₂ reduction, *Chem. Soc. Rev.* 52 (2023) 4343–4380.
- [5] I. Masood ul Hasan, L. Peng, J. Mao, R. He, Y. Wang, J. Fu, N. Xu, J. Qiao, Carbon-based metal-free catalysts for electrochemical CO₂ reduction: activity, selectivity, and stability, *Carbon Energy* 3 (2020) 24–49.
- [6] M. Wang, J. Luo, A coupled electrochemical system for CO₂ capture, conversion and product purification, *eScience* 3 (2023) 100155.
- [7] M. Liu, M. Peng, B. Dong, Y. Teng, L. Feng, Q. Xu, Explicating the role of metal centers in porphyrin-based MOFs of PCN-222(M) for electrochemical reduction of CO₂, *Chin. J. Struct. Chem.* 41 (2022) 2207046.
- [8] S. Nitopi, E. Bertheussen, S.B. Scott, X. Liu, A.K. Engstfeld, S. Horch, B. Seger, I.E. L. Stephens, K. Chan, C. Hahn, J.K. Norskov, T.F. Jaramillo, I. Chorkendorff, Progress and perspectives of electrochemical CO₂ reduction on copper in aqueous electrolyte, *Chem. Rev.* 119 (2019) 7610–7672.
- [9] H. Zhang, X. Wang, C. Chen, X. Yang, C. Dong, Y. Huang, X. Zhao, D. Yang, Selective CO₂-to-formic acid electrochemical conversion by modulating electronic environment of copper phthalocyanine with defective graphene, *Chin. J. Struct. Chem.* 42 (2023) 100089.
- [10] X. Zheng, P. De Luna, F.P. García de Arquer, B. Zhang, N. Beck-nell, M.B. Ross, Y. Li, M.N. Banis, Y. Li, M. Liu, O. Voznyy, C.T. Dinh, T. Zhuang, P. Stadler, Y. Cui, X. Du, P. Yang, E.H. Sargent, Sulfur-Modulated Tin Sites Enable Highly Selective Electrochemical Reduction of CO₂ to Formate, *Joule* 1 (2017) 794–805.
- [11] X. Liu, S. Zhang, S. Guo, B. Cai, S. Yang, F. Shan, M. Pumera, H. Zeng, Advances of 2D bismuth in energy sciences, *Chem. Soc. Rev.* 49 (2020) 263–285.
- [12] C. Peng, S. Yang, G. Luo, S. Yan, N. Chen, J. Zhang, Y. Chen, X. Wang, Z. Wang, W. Wei, T.-K. Sham, G. Zheng, Ampere-level CO₂-to-formate electrosynthesis using highly exposed bismuth (110) facets modified with sulfur-anchored sodium cations, *Chem* 9 (2023) 2830–2840.
- [13] M. Zhang, J. Wang, X. Rong, X. Lu, T. Lu, Surface iodine and pyrenyl-graphdiyne co-modified Bi catalysts for highly efficient CO₂ electroreduction in acidic electrolyte, *Nano Res.* (2023), <https://doi.org/10.1007/s12274-023-6073-4>.
- [14] Y. Li, J. Chen, S. Chen, X. Liao, T. Zhao, F. Cheng, H. Wang, In situ confined growth of bismuth nanoribbons with active and robust edge sites for boosted CO₂ electroreduction, *ACS Energy Lett.* 7 (2022) 1454–1461.
- [15] G. Zeng, Y. He, D. Ma, S. Luo, S. Zhou, C. Cao, X. Li, X. Wu, H. Liao, Q. Zhu, Reconstruction of ultrahigh-aspect-ratio crystalline bismuth-organic hybrid nanobelts for selective electrocatalytic CO₂ reduction to formate, *Adv. Funct. Mater.* 32 (2022) 2201125.
- [16] K. Fan, Y. Jia, Y. Ji, P. Kuang, B. Zhu, X. Liu, J. Yu, Curved surface boosts electrochemical CO₂ reduction to formate via bismuth nanotubes in a wide potential window, *ACS Catal.* 10 (2019) 358–364.
- [17] F. Yang, A.O. Elnabawy, R. Schimmenti, P. Song, J. Wang, Z. Peng, S. Yao, R. Deng, S. Song, Y. Lin, M. Mavrikakis, W. Xu, Bismuthene for highly efficient carbon dioxide electroreduction reaction, *Nat. Commun.* 11 (2020) 1088.
- [18] C. Lin, Y. Liu, X. Kong, Z. Geng, J. Zeng, Electrodeposited highly-oriented bismuth microparticles for efficient CO₂ electroreduction into formate, *Nano Res.* 15 (2022) 10078–10083.
- [19] M. Zhang, W. Wei, S. Zhou, D. Ma, A. Cao, X. Wu, Q. Zhu, Engineering a conductive network of atomically thin bismuthene with rich defects enables CO₂ reduction to formate with industry-compatible current densities and stability, *Energy Environ. Sci.* 14 (2021) 4998–5008.
- [20] L. Lv, R. Lu, J. Zhu, R. Yu, W. Zhang, E. Cui, X. Chen, Y. Dai, L. Cui, J. Li, L. Zhou, W. Chen, Z. Wang, L. Mai, Coordinating the edge defects of bismuth with sulfur for enhanced CO₂ electroreduction to formate, *Angew. Chem. Int. Ed.* 62 (2023) 202303117.
- [21] S. Chen, X. Li, C. Kao, T. Luo, K. Chen, J. Fu, C. Ma, H. Li, M. Li, T. Chan, M. Liu, Unveiling proton-feeding effect in sulfur-doped Fe-N-C single-atom catalyst for enhanced CO₂ electroreduction, *Angew. Chem. Int. Ed.* 61 (2022) e202206233.
- [22] W. Ma, S. Xie, X. Zhang, F. Sun, J. Kang, Z. Jiang, Q. Zhang, D. Wu, Y. Wang, Promoting electrocatalytic CO₂ reduction to formate via sulfur-boosting water activation on indium surfaces, *Nat. Commun.* 10 (2019) 892.
- [23] G. Chen, Y. Yu, K. Zheng, T. Ding, W. Wang, Y. Jiang, Q. Yang, Fabrication of ultrathin Bi₂S₃ nanosheets for high-performance, flexible, visible-NIR photodetectors, *Small* 11 (2015) 2848–2855.
- [24] R.M. Clark, J.C. Kotsakidis, B. Weber, K.J. Berean, B.J. Carey, M.R. Field, H. Khan, J.Z. Ou, T. Ahmed, C.J. Harrison, I.S. Cole, K. Latham, K. Kalantar-zadeh, T. Daeneke, Exfoliation of quasi-stratified Bi₂S₃ crystals into micron-scale ultrathin corrugated nanosheets, *Chem. Mater.* 28 (2016) 8942–8950.
- [25] L. Jia, M. Sun, J. Xu, X. Zhao, R. Zhou, B. Pan, L. Wang, N. Han, B. Huang, Y. Li, Phase-dependent electrocatalytic CO₂ reduction on Pd₃Bi nanocrystals, *Angew. Chem. Int. Ed.* 60 (2021) 21741–21745.
- [26] C. Cao, D. Ma, J. Gu, X. Xie, G. Zeng, X. Li, S. Han, Q. Zhu, X. Wu, Q. Xu, Metal-organic layers leading to atomically thin bismuthene for efficient carbon dioxide electroreduction to liquid fuel, *Angew. Chem. Int. Ed.* 59 (2020) 15014–15020.
- [27] P. Deng, F. Yang, Z. Wang, S. Chen, Y. Zhou, S. Zaman, B. Xia, Metal-organic framework-derived carbon nanorods encapsulating bismuth oxides for rapid and selective CO₂ electroreduction to formate, *Angew. Chem. Int. Ed.* 59 (2020) 10807–10813.
- [28] S. Liu, Y. Fan, Y. Wang, S. Jin, M. Hou, W. Zeng, K. Li, T. Jiang, L. Qin, Z. Yan, Z. Tao, X. Zheng, C. Shen, Z. Liu, T. Ah-mad, K. Zhang, W. Chen, Surface-oxygen-rich Bi@C nanoparticles for high-efficiency electroreduction of CO₂ to formate, *Nano Lett.* 22 (2022) 9107–9114.
- [29] J. Duan, T. Liu, Y. Zhao, R. Yang, Y. Zhao, W. Wang, Y. Liu, H. Li, Y. Li, T. Zhai, Active and conductive layer stacked superlattices for highly selective CO₂ electroreduction, *Nat. Commun.* 13 (2022) 2039.
- [30] L. Zhan, Y. Wang, M. Liu, X. Zhao, J. Wu, X. Xiong, Y. Lei, Hydropathy modulation on Bi₂S₃ for enhanced electrocatalytic CO₂ reduction, *Rare Met.* 42 (2023) 806–812.
- [31] P. Deng, H. Wang, R. Qi, J. Zhu, S. Chen, F. Yang, L. Zhou, K. Qi, H. Liu, B. Xia, Bismuth oxides with enhanced bismuth-oxygen structure for efficient electrochemical reduction of carbon dioxide to formate, *ACS Catal.* 10 (2019) 743–750.
- [32] M. Wang, S. Liu, B. Chen, M. Huang, C. Peng, Co-regulation of intermediate binding and water activation in sulfur-doped bismuth nanosheets for electrocatalytic CO₂ reduction to formate, *Chem. Eng. J.* 451 (2023) 139056.
- [33] M. Chen, S. Wan, L. Zhong, D. Liu, H. Yang, C. Li, Z. Huang, C. Liu, J. Chen, H. Pan, D. Li, S. Li, Q. Yan, B. Liu, Dynamic restructuring of Cu-doped SnS₂ nanoflowers for highly selective electrochemical CO₂ reduction to formate, *Angew. Chem. Int. Ed.* 60 (2021) 26233–26237.
- [34] X. Yang, Q. Wang, F. Chen, H. Zang, C. Liu, N. Yu, B. Geng, In-situ electrochemical restructuring of Cu₂Bi₂S_x solid solution into Bi/Cu₃S_y heterointerfaces enabling stabilization intermediates for high-performance CO₂ electroreduction to formate, *Nano Res.* 16 (2023) 7974–7981.
- [35] M. Zhao, Y. Gu, W. Gao, P. Cui, H. Tang, X. Wei, H. Zhu, G. Li, S. Yan, X. Zhang, Z. Zou, Atom vacancies induced electron-rich surface of ultrathin Bi nanosheet for efficient electrochemical CO₂ reduction, *Appl. Catal. B: Environ.* 266 (2020) 118625.
- [36] R. Pang, P. Tian, H. Jiang, M. Zhu, X. Su, Y. Wang, X. Yang, Y. Zhu, L. Song, C. Li, Tracking structural evolution: operando regenerative CeO_x/Bi interface structure for high-performance CO₂ electroreduction, *Nat. Sci. Rev.* 8 (2021) 187.
- [37] C. Zhang, X. Hao, J. Wang, X. Ding, Y. Zhong, Y. Jiang, M.-C. Wu, R. Long, W. Gong, C. Liang, W. Cai, J. Low, Y. Xiong, Concentrated formic acid from CO₂ electrolysis for directly driving fuel cell, *Angew. Chem. Int. Ed.* (2024), <https://doi.org/10.1002/anie.202317628>.
- [38] P.-F. Sui, M.-R. Gao, R. Feng, S. Liu, J.-L. Luo, Unveiling phase-selective α- and β-Bi₂O₃-derived electrocatalysts for CO₂ electroreduction, *Chem. Catal.* 3 (2023) 100842.
- [39] S. Zhao, Y. Qin, X. Wang, C. Wang, X. Chen, Y. Wang, J.X. Yu, X. Liu, Y. Wu, Y. Chen, Anion exchange facilitates the in situ construction of Bi/Bi-O interfaces for enhanced electrochemical CO₂-to-formate conversion over a wide potential window, *Small* 19 (2023) 2302878.
- [40] G. Jia, Y. Wang, M. Sun, H. Zhang, L. Li, Y. Shi, L. Zhang, X. Cui, T.W.B. Lo, B. Huang, J.C. Yu, Size effects of highly dispersed bismuth nanoparticles on electrocatalytic reduction of carbon dioxide to formic acid, *J. Am. Chem. Soc.* 145 (2023) 14133–14142.
- [41] B. Wulan, L. Zhao, D. Tan, X. Cao, J. Ma, J. Zhang, Electrochemically driven interfacial transformation for high-performing solar-to-fuel electrocatalytic conversion, *Adv. Energy Mater.* 12 (2022) 2103960.
- [42] Y. Hori, A. Murata, R. Takahashi, Formation of hydrocarbons in the electrochemical reduction of carbon dioxide at a copper electrode in aqueous solution, *J. Chem. Soc. Faraday Trans.* 85 (1989) 2309–2326.